Thermal performance assessment of the world's first solar thermal Fresnel lens collector field

Adam R. Jensen [a,*], Ioannis Sifnaios [a], Gideon P. Caringal [b], Simon Furbo [a], Janne Dragsted [a]

[a] *Department of Civil Engineering, Technical University of Denmark, Brovej, Building 118, 2800 Kgs. Lyngby, Denmark*
[b] *Heliac A/S, Savsvinget 4D, 2970 Hørsholm, Denmark*

ARTICLE INFO

ABSTRACT

Fresnel lenses are used in a wide range of solar energy applications, primarily due to their reduced material usage, low cost, and high optical efficiency. This study presents an investigation of the world's first full-scale Fresnel lens solar collector field. The collector field consists of 144 two-axis tracking solar collectors manufactured by the Danish company Heliac and supplies heat to the local district heating network in Lendemarke, Denmark. The thermal performance of the solar collector field was determined using the quasi-dynamic test method. It was found that the peak efficiency was 11% lower compared to a brand-new collector and that heat losses from the collectors made up half of the total heat losses of the solar field. The reduction in the peak efficiency was primarily caused by soiling as the collectors were exposed to outdoor conditions for one year without cleaning. Furthermore, the system's annual performance was determined using a simulation model developed in TRNSYS and validated by comparison to measurement data. For 2020, the heat generation was 373 kWh/m^2 (relative to aperture area) when operating with an outlet temperature of 90 °C and inlet temperature of 50 °C. Additionally, a sensitivity analysis of the annual heat generation was performed, varying the ground cover ratio, mean collector temperature, and soiling level. The sensitivity analysis showed that the heat generation was relatively insensitive to changes in the mean collector temperature, demonstrating that the collectors are suitable for generating heat above 100 °C, unlike flat-plate collectors.

1. Introduction

Similar to conventional lenses, Fresnel lenses function based on the principle of refraction. However, Fresnel lenses require significantly less material than conventional lenses, as they utilize many small concentric or parallel prisms. The sunlight passes through the lens and is refracted towards the focus point/line as each prism approximates the refraction angle of a conventional continuous surface lens.

The first documented use of Fresnel lenses was in 1822 as a collimator for a lighthouse by Augustin Jean Fresnel, who is generally accredited with their invention (Leutz and Suzuki, 2001). However, it was first with the development of polymer Fresnel lenses by Miller et al. (1951) that Fresnel lenses achieved widespread usage and research attention. Since then, Fresnel lenses have been used for a wide range of applications, including several within the field of solar energy, such as solar thermal collectors (Perini et al., 2017), concentrated photovoltaics (Yamaguchi et al., 2005), and solar lighting (Tsangrassoulis et al., 2005).

Fresnel lenses represent a promising alternative to mirrors for concentrating solar collectors, as they are lightweight, robust, noncorroding, and cheap to manufacture (Kumar et al., 2015). Solar collectors based on Fresnel lenses can be divided into two categories: point focusing collectors – which are suitable for high-temperature applications but require two-axis tracking – and line-focusing collectors – which are limited to medium temperature applications but only require one-axis tracking (Xie et al., 2011).

Within these two categories, many different designs of Fresnel lens collectors have been proposed. For example, Wang et al. (2018) developed a point-focusing Fresnel lens collector with a concentration ratio of 500. The optical efficiency of the lens was determined experimentally to be greater than 71.6%. Lin et al. (2014) investigated the impact of receiver design for Frenel lens collectors and determined the optical efficiency of a collector with a triangular and rectangular cavity receiver to be 69.8% and 61.8%, respectively. Simulations carried out in the same study were found to overestimate the optical efficiency significantly, partly attributed to simulations not accounting for manufacturing imperfections of the lens. A comparative study of point-

---

Nomenclature

Latin letters

A	Collector aperture area [m²]
a_1	Heat loss coefficient [W/(m² K)]
a_2	Temperature dependence of the heat loss coefficient [W/(m² K²)]
a_3	Wind speed dependence of the heat loss coefficient [J/(m³ K)]
a_4	Sky temperature dependence of the heat loss coefficient [-]
a_5	Effective thermal capacity [J/(m² K)]
a_6	Wind speed dependence of the zero loss efficiency [s/m]
a_7	Wind speed dependence of IR radiation exchange [s/m]
a_8	Radiation losses [W/(m² K⁴)]
c_p	Specific heat capacity of heat transfer fluid [J/(kg K)]
E_L	Longwave irradiance ($\lambda > 3\ \mu m$) [W/m²]
G_b	Direct solar irradiance (beam irradiance) [W/m²]
G_d	Diffuse solar irradiance [W/m²]
G_{hem}	Hemispherical irradiance [W/m²]
K_b	Incidence angle modifier for beam irradiance [-]
K_d	Incidence angle modifier for diffuse irradiance [-]

$\dot{Q}$	Useful power extracted from collectors [W]
t	Time [s]
T_a	Sky temperature (absolute) [K]
T_{amb}	Ambient air temperature [°C]
$T_{forward}$	District heating forward temperature [°C]
T_{in}	Collector field inlet temperature [°C]
T_{mean}	Mean temperature of heat transfer fluid [°C]
T_{out}	Collector field outlet temperature [°C]
T_{return}	District heating return temperature [°C]
u'	Reduced surrounding air speed [m/s]
$\dot{V}$	Volumetric flow [m³/s]

Greek letters

$\eta_{0,b}$	Peak collector efficiency (at $T_{mean} - T_{amb} = 0$ K) based on beam irradiance G_b [-]
θ_L	Longitudinal incidence angle [°]
θ_T	Transversal incidence angle [°]
ρ	Density of heat transfer fluid [kg/m³]
σ	Stefan-Boltzmann constant [W/(m² K⁴)]

---

focusing and linear-focusing Fresnel lenses was carried out by Imtiaz Hussain and Lee (2016), who analyzed two collectors with the same area and found that the point-focusing collector had a 7% higher average efficiency.

Additionally, the theoretical performance of a linear Fresnel lens collector was investigated by Ibrahim and Sakhrieh (2016) using ray-tracing. The study reported a peak efficiency of 77.3%, exceeding that of typical parabolic trough collectors. More recently, Perini et al. (2017) constructed and investigated a two-axis tracking Fresnel lens solar collector. The overall efficiency of the collector was less than 20% due to a poor lens design leading to high optical losses (47% of total losses) and a low absorptance of the receiver (33% of total losses). In contrast, Zhai et al. (2010) presented an experimental investigation of a linear Fresnel lens collector with a peak efficiency of 56.9% and an overall efficiency of 50% at a mean temperature of 90 °C.

While numerous studies have investigated individual Fresnel lens solar collectors experimentally and theoretically, there have not yet been any full-scale systems (unlike Fresnel reflector collectors). Thus, when the world's first Fresnel lens solar collector field was inaugurated in Lendemarke, Denmark, in 2018, it created a unique opportunity to study Fresnel lens solar collectors on a large scale.

This study presents an investigation of the Lendemarke Fresnel lens collector field and a characterization of the system's thermal performance using the quasi-dynamic test (QDT) method. To analyze the annual performance of the system, a simulation model was developed and validated. Additionally, the study presents a sensitivity analysis of the annual yield with respect to variations in ground cover ratio, soiling, and mean collector temperature.

The remainder of the paper is structured as follows: Section 2 introduces the methods as well as a detailed description of the plant, Section 3 presents the results, and Section 4 gives the conclusions of the study.

2. Methods
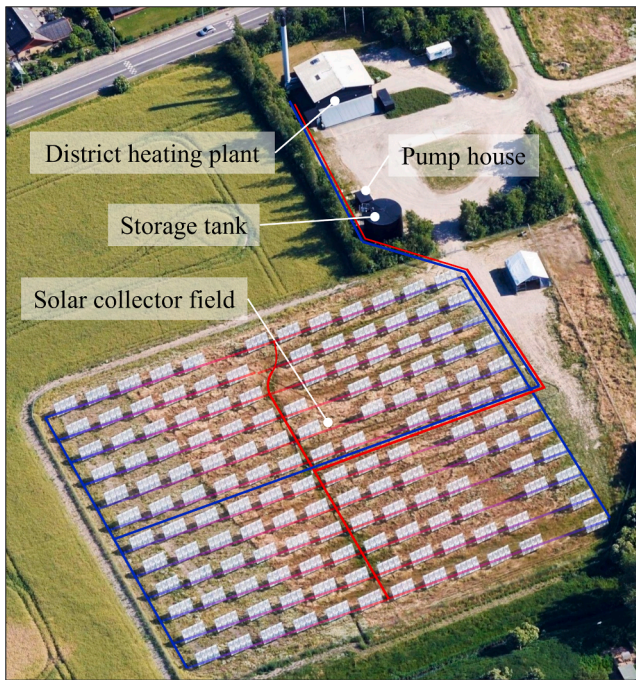
2.1. Lendemarke solar field

The Lendemarke solar collector field consists of 144 two-axis tracking Fresnel lens solar collectors manufactured by the Danish company Heliac. The solar field spans 1 ha and is located outside the town of Lendemarke on the island of Møn, Denmark (latitude: 54.9788°N, longitude: 12.2666°E). A photo of the collector field during operation is shown in Fig. 1.

The heat generated from the collector field is supplied to the

Fig. 1. Photo of the Fresnel lens solar collector field in Lendemarke, Denmark during operation. The white spot in the receiver boxes is the focus point of the lenses. The photo was taken when the field was inaugurated and the pipes have since been insulated.

Fig. 2. Aerial view of the Lendemarke solar collector field and district heating plant. Colored lines illustrate the piping network. Image source: the Danish Agency for Data Supply and Efficiency.

Fig. 3. Illustration of the Heliac concentrating solar collector. Fresnel grooves are enhanced for visualization.

accumulation tank of the local district heating plant (see Fig. 2). In addition to the solar field, the plant consists of a 2 MW biomass boiler, a 3.7 MW backup oil boiler, and a 400 m³ storage tank. The town's 335 consumers are connected with 13 km of pipes and have an average annual heating demand of 8900 MWh. Compared to other district heating plants in Denmark, the plant is relatively small and is atypical in that it does not generate electricity (i.e., combined heat and power), which is generally required by law.

The Heliac solar collector, illustrated in Fig. 3, is a point-focusing collector that concentrates the direct solar radiation by means of eight Fresnel lenses (approx. 2 m² each). The polymer film Fresnel lenses are applied to the backside of a float glass and can be made at a very low cost due to a novel roll-to-roll manufacturing process. The lenses are manufactured using a commercial roll-to-roll process known as extrusion coating, where a polymer melt is structured by a cooling roller as the melt is laminated onto a carrier foil. Present equipment allows for foil production at 5 m²/s, equal to potentially 100 GW a year.

A square receiver is positioned at the focus point of each Fresnel lens. The lenses, receivers, and piping are mounted on a two-axis solar tracker, which continuously aligns the collector normal to the sun. The solar trackers are pile-founded and feature two slewing drives and a control unit, which calculates the solar position with an accuracy of 0.1°. The trackers have a full tilt range (0–90°) and azimuth range of 285°. Each collector has a total aperture area of 16.55 m², a maximum height of 3.5 m, and a maximum operating temperature of 110 °C.

Each receiver measures 24 by 24 cm, resulting in a concentration ratio of 36. The receivers are coated with a high-temperature refractory paint with an absorptivity of 97% and made of stainless steel to withstand the high temperatures occurring at the focus point. To limit heat losses, the backside of each receiver is insulated, and the front is enclosed by a cover glass. Both sides of the receiver cover glass and the front side of the float glass are treated with an anti-reflective coating. Heat is transferred to a heat transfer fluid, which is circulated through the receivers. The eight receivers are serially connected with insulated stainless steel pipes.

As early versions of the Fresnel lens had a lifetime of less than a year, all lenses were changed to an improved version in May 2020. The new version of the lens has an expected lifetime of more than five years. Research is ongoing to further extend the lifetime, partly by carrying out accelerated UV tests to elucidate the lens degradation. The receivers and cover glass had not been replaced since the plant's construction in 2018 and therefore had been exposed to outdoor conditions for three years. The receiver with the cover glass is shown in Fig. 4.

The solar collectors are organized in a square layout, meaning there is an equal distance (8 m) between the trackers in the row and the column directions. This layout arrangement corresponds to a ground cover ratio (GCR) of 0.26. The field deviates slightly from the aforementioned configuration, as it was necessary to increase the distance between some trackers to maintain a safe distance to an underground wastewater pipe that runs through the field. An illustration of the field piping is shown in Fig. 2. The cold heat transfer fluid enters from the edges of the field and flows through six collectors connected in series. This way, the piping that carries the hot fluid is minimized.

2.2. Measurement equipment

The heat generated from the solar collector field, $\dot{Q}$, can be calculated as:

$$\dot{Q} = \dot{V}(T_{out} - T_{in})c_p \, \rho \tag{1}$$

where $\dot{V}$ is the volume flow rate, c_p is the specific heat capacity, and ρ is the density of the heat transfer fluid. T_{in} and T_{out} are the inlet and outlet temperatures measured after and before the heat exchanger on the primary side, respectively.

Fig. 4. Close-up photo of the receiver box.

The flow rate and temperatures were measured in the pump house shown in Fig. 2. The flow rate was measured with a Woltman flow meter manufactured by GWF MessSysteme AG with a stated uncertainty of less than 1%. The temperatures were measured using PT100 immersion sensors. The uncertainty of the relative temperature measurement (between the inlet and outlet) is estimated to be 0.2 K. The specific heat capacity is evaluated at the mean temperature, whereas the density is evaluated at the outlet temperature as the flow meter is mounted in the outlet pipe. Due to the use of glycol, the combined uncertainty of the heat generation is estimated to be 4%.

The direct normal irradiance (DNI), also called beam irradiance, was measured using a Kipp & Zonen SHP1 Class-A pyrheliometer. The pyrheliometer was mounted on a Kipp & Zonen RaZON + solar tracker. The uncertainty of the pyrheliometer was estimated to be less than 0.5% by comparison to the World Standard Group during the 13th International Pyrheliometer Comparison (IPC-XIII) in 2021 in Davos, Switzerland.

Wind measurements from the site were made at a height of 5 m, using a WS50 cup anemometer with an estimated uncertainty of 1.5 m/s. The air temperature at 2 m was obtained from ECMWF's ERA5 reanalysis dataset (Hersbach et al., 2018), as the local air temperature measurements were affected by solar radiation. The ERA5 dataset combines model data obtained from weather forecast models and observations. The accuracy of the air temperature retrieved from ERA5 was assessed by comparison to measurements for 2020 from the nearby meteorological station Vindebæk Kyst operated by the Danish Meteorological Institute (DMI). The comparison showed an excellent agreement, with ERA5 exhibiting a small bias of 0.27 K and a root mean square deviation (RMSD) of 1.2 K.

The system pressure was measured before and after the heat exchanger and after the pump. The pressure measurements were made in the pump house using piezoresistive pressure sensors (Danfoss MBD 3200) with an uncertainty of 1%.

2.3. The QDT equation

Concentrating solar thermal collectors are generally characterized using the quasi-dynamic test (QDT) method, as prescribed by the international standard ISO 9806 (International Organization for Standardization, 2017). While the method was developed for testing individual collectors, it can also be applied to collector fields with slight modifications (Sallaberry et al., 2019).

The QDT method describes the expected heat generation ($\dot{Q}_{modeled}$) as:

$$\frac{\dot{Q}_{modeled}}{A} = \eta_{0,b}\ K_b(\theta_L, \theta_T)G_b + K_d\ \eta_{0,b}\ G_d$$

$$- a_1(T_{mean} - T_{amb})$$

$$- a_2(T_{mean} - T_{amb})^2$$

$$- a_3\ \dot{u}\ (T_{mean} - T_{amb})$$

$$+ a_4\big(E_L - \sigma\ T_a^4\big)$$

$$- a_5\ dT_{mean}/dt$$

$$- a_6\ \dot{u}\ G_{hem}$$

$$- a_7\ \dot{u}\ \big(E_L - \sigma\ T_a^4\big)$$

$$- a_8(T_{mean} - T_{amb})^4 \tag{2}$$

where G_b and G_d are the beam and diffuse irradiances, respectively, A is the collector aperture area, and u' is the reduced wind speed. T_{mean} is the mean collector fluid temperature, T_{amb} is the ambient air temperature,

and dT_{mean}/dt is the time derivative of T_{mean}. $K_b(\theta_L, \theta_T)$ is the incidence angle modifier for the direct irradiance, which can be set to one as the tracker is always maintained normal to the sun. For a detailed description of the variables, the reader is referred to ISO 9806.

Parameters $\eta_{0,b}$, K_b, K_d, and a_1 through a_8 are constants that describe the heat gain and loss characteristics of the specific collector or system, normalized by the collector area. For collectors with a concentration ratio greater than 20, which is the case of the Heliac collector, the coefficients a_2, a_3, a_4, a_6, a_7, and K_d may be set to zero. The relevant coefficients are determined by statistical least-square fitting of Eq. (2) to measurement data. Measurements from 10 days between March 15th and April 10th, 2021, were used, as the plant operated continuously during this period, and DNI measurements were available. For comparison, the results will be compared to the coefficients of a single Heliac collector, which were derived under controlled conditions and documented in (Jensen, 2020).

2.4. Modeling

To investigate the annual performance of the collector field, a simulation model was developed since the plant had not been operating continuously for a full year due to multiple periods where it was taken out of operation for service. The simulation model was created using the TRNSYS simulation program, and a schematic of the model is shown in Fig. 5. The collector field was modeled using TESS Type 1290, which models the solar collector field similarly to Eq. (2). In addition to the field performance coefficients, Type 1290 requires the input of the ambient temperature, wind speed, incident irradiance, and inlet temperature.

There are two options for specifying the solar collector field flow rate: using Type 1290's built-in flow controller or passing in the flow rate externally. For the validation of the model, the measured flow rate was supplied to the collector component, whereas for the annual simulations, the flow rate was determined using the built-in flow controller.

The built-in flow controller modulates the flow rate in order to keep the outlet temperature as close as possible to the desired setpoint, though within the range of the specified minimum and maximum flow rates. Additionally, the controller turns off the collector (zero flow) if heat is lost, corresponding to defocusing of the collectors. The minimum flow rate was set to 9 m³/h to avoid overheating, and the maximum was set to 32 m³/h, corresponding to the maximum flow rate of the pump.

The model also accounts for the interconnection of the solar collector field with the district heating plant through a heat exchanger located in the pump house. The heat exchanger is a counter-flow plate heat exchanger with an effective heat transfer area of 66.6 m² and an overall heat transfer coefficient of 2859 W/(m² K).

Shading of the solar collectors due to self-shading was accounted for using the algorithms from Jensen et al. (2022). The field layout was specified with a GCR of 0.26, a counterclockwise rotation of 22°, an aspect ratio of one, and an offset of zero. For a detailed description of field layout parameters, the reader is referred to Cumpston and Pye (2014). The shading fraction for each time step was determined, taking
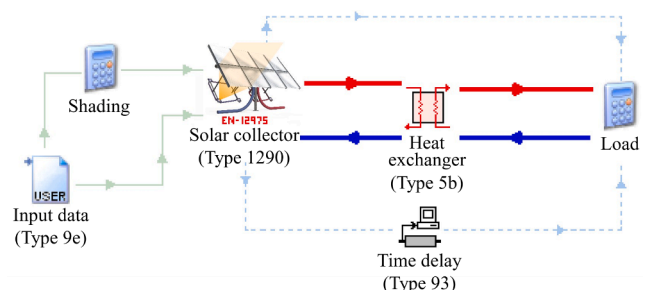

Fig. 5. Schematic of the simulation model in TRNSYS.

into account second-order neighboring collectors.

The annual simulation was carried out for 2020, as this was the most recent complete year. The ambient temperature, T_{amb}, was acquired from ERA5, and modeled irradiance data was obtained from the CAMS Radiation Service (Qu et al., 2016). A validation study of the CAMS Radiation Service by Wald and Lefévre (2018) showed that the bias of the hourly direct normal irradiance was between –7% and 2.5% for the 12 investigated sites, and the RMSD ranged from 8.2% to 14.1%. A simulation time step of 15-min was used. The return temperature from the heating network, T_{return}, was assumed to be 50 °C for the entire period, and the setpoint outlet temperature from the solar collector field was set to 90 °C.

The flow rate on the district heating side of the heat exchanger (secondary side) was determined using a feedforward controller. The controller calculates the flow rate based on Eq. (1), where the $\dot{Q}$ is taken as the heat generation of the solar field at the previous time step. This is achieved using the Type 93 delay component. T_{out} is, in this case, the forward temperature, $T_{forward}$, to the district heating grid and is set to 10 K less than the collector field outlet temperature.

The collector field heat generation is relatively small compared to the district heating load. For this reason, the remaining system was not modeled as it was assumed that the heat produced by the collector field could always be supplied directly to the district heating network.

2.5. Sensitivity analysis

A sensitivity analysis was carried out to investigate how the annual heat generation is affected by key parameters. The analysis was accomplished using the developed simulation model and assessing the impacts of variations in soiling level, outlet temperature, and ground cover ratio on the annual heat generation. The soiling level was varied between 0% (clean) and 11%, the solar collector outlet temperatures between 70 and 110 °C, and ground cover ratios between 0.1 and 0.35. The GCR values were chosen to cover the range of common field layouts.

3. Results

3.1. Field performance

An example of the system performance during the course of one day is shown in Fig. 6, including the heat generation, measured and modeled DNI, system temperatures, and flow rate. From the irradiance profile, it is evident that the day was cloud-free. Direct irradiance was detected around 6:10, whereas sunrise was at 4:54. Heat generation first started around 6:50, before which the system was heating up, as seen from the increasing temperatures in the third subplot.

Generally, the temperatures were relatively stable throughout the day, except for a spike between 9 and 10:30 am. The spike in temperature was caused by an increase in the temperature on the secondary side, as the biomass plant was also running and the tank was fully charged. This, in turn, lowered the heat transfer in the heat exchanger and increased the temperature in the collector field. Otherwise, small variations in the solar collector outlet temperature are noticeable. However, when comparing the outlet temperature on the secondary side ($T_{forward}$), it can be seen that the temperature variations are eliminated due to the flow control on the secondary side.

Another important parameter to consider is the system pressure drop, which is shown as a function of flow rate in Fig. 7. Erroneous data and periods of unstable operation have been filtered out; otherwise, all hours between February and September 2021 are shown.

For comparison, the pressure drop of six Heliac collectors in series based on Jensen (2020) is also shown by the red curve in Fig. 7. The measured pressure drop of the collector field is approximately 1.5 times higher than the pressure drop of just the collectors, meaning two-thirds of the pressure drop is due to the collectors. The remaining third is due to
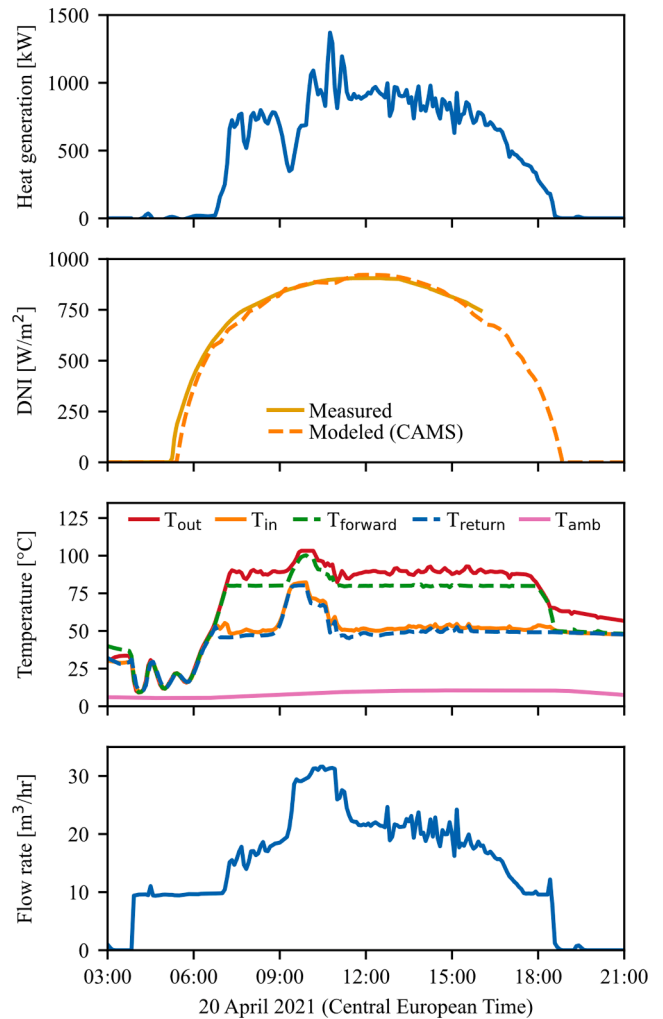

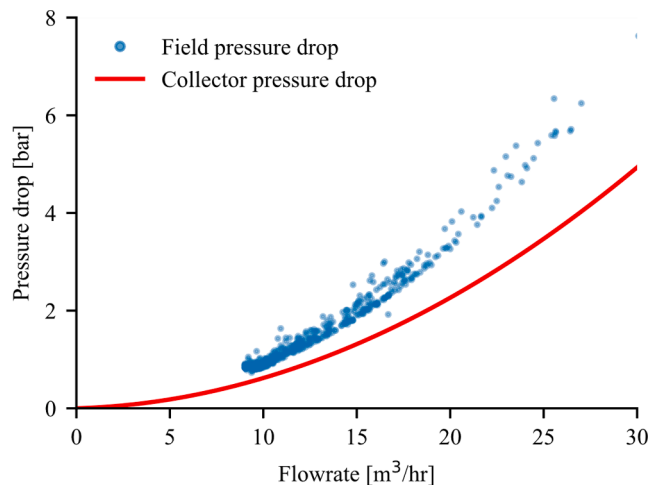**Fig. 6.** Measurements from the solar field during April 20th, 2021.

Fig. 7. Comparison of the measured pressure drop in the solar collector field and the contribution of just the collectors. Each dot is the hourly average pressure drop for one hour.

the piping between collectors and piping between the collector field and pump house.

The pressure drop is an order of magnitude larger than similar-sized flat-plate collector fields. For example, a 3024 m² flat-plate collector

field in Høje Taastrup, Denmark, had six collectors in series and a pressure drop of 0.6 bar at 25 m³/h (Bava et al., 2017). The large pressure drop in the collector field is a significant drawback, as it limits the number of collectors that can be connected in series and increases the electricity consumption of the pump.

Approximately 40% of the pressure drop in the collector occurs in the receivers. However, a new receiver design has been proposed with a 20% reduction in pressure drop and a smaller size to reduce heat losses. The new receiver design will be used for future systems, including a new plant of 144 trackers currently under construction in Hørsholm, Denmark. Additionally, most pipes in the new plant will be smooth pipes leading to a lower pressure drop, whereas the pipes used in Lendemarke were primarily corrugated.

3.2. Performance coefficients

The QDT characterization of the solar collector field resulted in a peak efficiency of 53.5%, a heat loss coefficient of 1.62 W/(m² K), and an effective thermal capacity of 11.5 kJ/(m² K). The values and their standard errors are listed in Table 1. As previously mentioned, only some of the coefficients in Equation (2) are applicable for concentrating collectors. Additionally, not all of the applicable parameters, e.g., a_8, were found to be statistically significant and were set to zero; thus, they were not included in Table 1.

For comparison, the performance coefficients derived for a single Heliac collector in (Jensen, 2020) are also presented in Table 1. It should be noted that these values are for a brand-new collector with water as the heat transfer fluid. The coefficients do not account for connecting pipes and soiling, as the tested collector was cleaned regularly during the testing period. The peak efficiency is expected to be lower under actual operation due to increased optical losses due to soiling. Also, the heat losses and thermal capacity are higher for the collector field due to additional piping.

The Lendemarke solar field's peak efficiency was 11% lower than the values provided in the single collector test report. This reduction is expected to be primarily caused by soiling, as the collectors had been exposed for more than one year without any cleaning. This is not surprising as concentrating solar collectors are known to be much more affected by soiling, sometimes 8–14 times more than PV panels (Bellmann et al., 2020). A soiling level of 11% is used for the remainder of this paper. The soiling level is defined as the reduction in the peak efficiency of the soiled collectors in Lendemarke compared to the laboratory test value. Thus the impact of soiling is quantified without considering the soiling type or distribution. Moreover, the use of water-glycol as the heat transfer fluid also slightly reduces the peak efficiency, as it reduces the receiver's heat removal factor. Additionally, the lenses installed at the site also had some manufacturing imperfections not present on the lenses used in the single collector test.

A number of different sources contribute to soiling, including settling of airborne dust particles, bird droppings, and algae growth. For the specific collector, soiling is most pronounced on the front side of the collector's float glass and the front side of the receiver cover glass, as these surfaces face upwards. Some soiling also occurs on the receiver surface, backside of the cover glass, and the Fresnel lens itself, which cannot easily be cleaned. Soiling of the receiver surface and the backside of the cover glass is possible as there is a gap between the receiver box and the cover glass (see Fig. 4).

The collector test report includes wind speed dependence of the heat loss coefficient (a_3), which was not found to be statistically significant for the characterization of the collector field. Therefore, for a fair comparison with the heat losses of the single collector, a_1 and a_3 should be combined. Assuming an average wind speed of 3 m/s gives an overall heat loss coefficient of 0.76 W/(m² K) for the collector. The heat loss coefficient for the field is approximately twice as high, meaning that the heat loss from the collector accounts for roughly half of the heat losses of the entire collector field, and the remaining heat losses are attributed to the field piping.

It should be noted that the uncertainty of the field coefficients is significantly higher than the collector coefficients. First, the uncertainty of the measurements from which the collector coefficients were derived was lower, and the testing was made under controlled conditions. Second, the heat transfer fluid in the field was water-glycol with additives, resulting in a higher uncertainty of the flow rate and the thermal properties. An additional source of uncertainty includes the limited range of operating conditions from which the field coefficients were derived, i.e., the mean operating temperature did not vary significantly for most days.

3.3. Model validation

A comparison of the modeled and measured heat generation and field outlet temperature is presented in Fig. 8. The figure shows the same day as in Fig. 6, but only for the period where there were valid DNI measurements. The modeled heat generation is in close agreement with the measured and within the error bars of the measured heat generation during most of the period. The only major exception is between 9 and 10 am, corresponding to the temperature spike in the system, where the model overestimates the heat generation. This shows that the model does not precisely capture the system dynamics during rapid temperature changes, although such events rarely occur under normal circumstances. The overestimation may be due to the underestimation of the system's thermal capacity and the long fluid residence time, which is not accounted for in the model. However, overall the simulation model performs well for the day.

For a general overview of the model performance, a scatter plot of the modeled vs. measured heat generation is shown in Fig. 9. The plot compares the same ten days used to derive the QDT coefficients but includes all data points between 9 am and 4 pm. Each point on the scatter plot corresponds to the average heat generation for one hour. The maximum hourly heat generation was 1034 kW. The plot shows only minor deviations, predicting well for hours with low and high production. Notably, the model has a tendency to overestimate the heat generation in the range of 600–900 kW and overall exhibits a positive bias of 1.8%.

Table 1

Solar collector field coefficients derived using the QDT method. The performance coefficients for a single collector are included for comparison. All coefficients are with respect to the aperture area.

Parameter	Description	Field coefficients	Std. error (field coef.)	Collector coefficients (Jensen, 2020)	Unit
$\eta_{0,b}$	Peak collector efficiency based on beam irradiance G_b	0.535	0.01	0.602	–
K_d	Diffuse incidence angle modifier	–	–	0.02	–
a_1	Heat loss coefficient	1.62	0.16	0.23	W/(m² K)
a_3	Wind dependence of the heat loss coefficient	–	–	0.178[*]	J/(m³ K)
a_5	Effective thermal capacity	11 500	1 000	3 360	J/(m² K)

[*] Collector coefficients were derived using the measured wind speed (non-reduced).
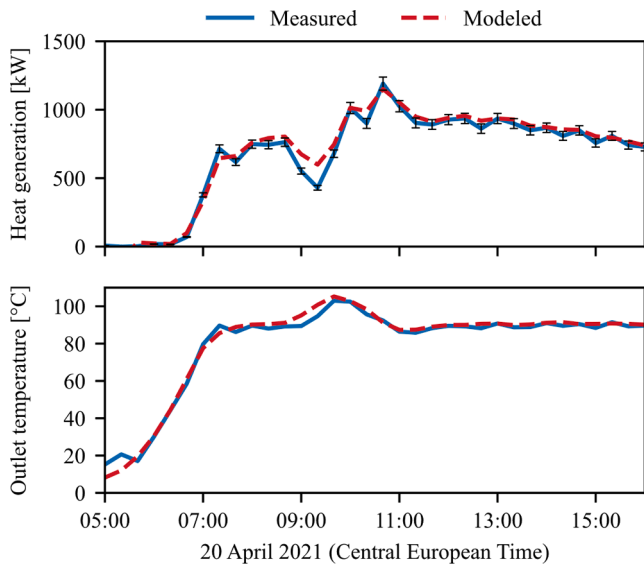
Fig. 8. Comparison of measured and modeled heat generation during one example day, using 20-minute data.
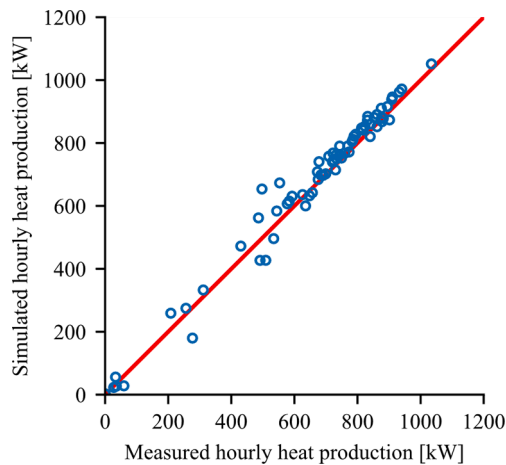

Fig. 9. Comparison of the measured and modeled average heat production on an hourly basis for the validation period. Only periods between 9 am and 4 pm are shown in order to exclude periods where the pyrheliometer might be shaded.

3.4. Annual performance

The monthly heat generation calculated using the model is shown in Fig. 10. Due to the relatively northern location, the heat generation exhibits a large seasonal variation, with essentially no heat generation during the winter months. The simulated year 2020, was characterized by a sunny spring and an annual direct irradiation of 1219 kWh/m^2.

The total heat generation of the collector field was 889 MWh for the entire year, corresponding to 373 kWh/m^2 with respect to the aperture area. This is approximately 10% of the annual heat demand of the town. The remaining heat is primarily generated by the biomass boiler and less than 1% from the oil boiler.

In comparison, a flat-plate collector field in the nearby town of Stege generated 477 kWh/m^2 during 2020. The collector field is located less than 3 km from the Lendemarke solar field and has an inlet and outlet temperature of 45 and 90 °C, respectively. Thus with the current plant configuration and local conditions, i.e., mean temperature of 70 °C and soiling level, the Heliac collector field generates less heat than a traditional flat-plate collector field. The impact of the main parameters is
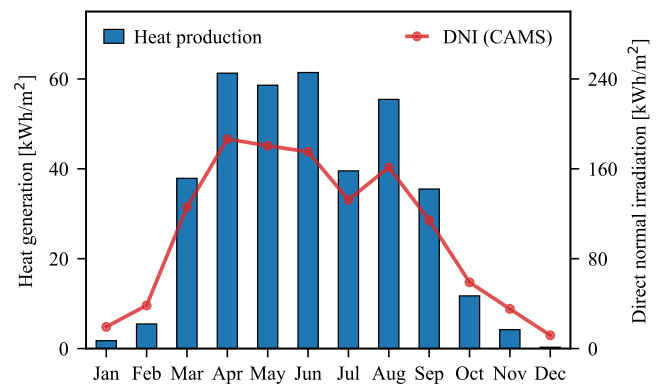

Fig. 10. Monthly heat generation and direct normal irradiation for the annual simulation.

investigated in the following section.

3.5. Sensitivity results

The annual simulation was based on the actual plant configuration and integration with the local district heating system, which will be used as the reference scenario in the sensitivity analysis. These parameters undoubtedly differ from site to site; hence it is interesting to elucidate how they affect heat generation and what annual performance can be expected for other systems.

For example, the annual simulation carried out using the performance coefficients presented in Section 3.2 includes the effects of the local soiling conditions. While soiling is inevitable, it varies strongly from location to location, and system operators can affect it by cleaning. Therefore, understanding the impact of soiling is essential to determining how often to clean, if at all.

For the sensitivity analysis, the reduction of the peak efficiency will be assumed to only be due to soiling, which is indeed the primary contributor. Therefore, simulations are carried out for cases ranging between the current conditions of 11% soiling ($\eta_{0,b} = 0.535$) and the case of no soiling ($\eta_{0,b} = 0.602$). The annual heat generation for the six simulated cases with varying soiling levels is presented in Fig. 11. The figure shows that under clean conditions, the heat generation would be 19.2% higher than at the current soiling level of 11%. This demonstrates that the soiling level has an amplified effect on the heat generation, i.e.,
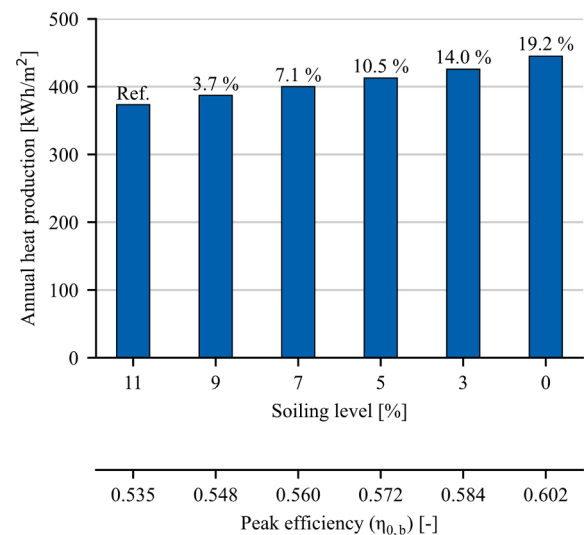

Fig. 11. Impact of soiling on the annual heat production. The percentages above each bar represent the deviation from the reference scenario.

the reduction in heat generation is almost twice the soiling level due to the heat losses remaining the same. Along with cost estimates of cleaning, this information is crucial in determining whether and how often to clean the collectors.

The choice of ground cover ratio is another parameter that has to be chosen from a cost-optimal perspective. A lower GCR means less shading (as collectors are further apart) and a higher thermal output but comes at the expense of greater land procurement costs. To elucidate the impact of shading, the annual heat generation is shown for six scenarios with GCRs ranging from 0.1 to 0.35 in Fig. 12. Only the impact of shading is accounted for and not the change in piping length. The plot shows that increasing the land area by 160% (from GCR 0.26 to 0.1) increases the heat generation by 6.5%. Conversely, when reducing the row spacing from 8 m to 7 m (26% reduction in land area; from GCR 0.26 to 0.35), the heat generation is reduced by 4.9%. It is crucial that these numbers are used in conjunction with projections of land costs during the design phase to achieve the lowest cost of energy.

Perhaps the most influential parameter is the average collector temperature, which is typically dictated by the application. The mean collector temperature is the dominant factor of heat losses, as evident from Eq. (2). The impact on the annual heat generation for the investigated mean/outlet temperatures is shown in Fig. 13. It can be seen that changing the outlet temperature by plus or minus 10 K changes the heat generation by −6.1 and 5.5%, respectively. While the heat generation does decrease with increasing mean temperature, it is much less affected than traditional flat-plate collectors. The heat generation from flat-plate collectors decreases at a much more significant rate and approaches zero for outlet temperatures above 100 °C (Tschopp et al., 2020). From this perspective, it is notable that the collector field would supply 327 kWh/m² at an outlet temperature of 110 °C. This is due to the low heat losses, which is a key advantage of concentrating collectors.

It should be considered that the version of the collector installed at Lendemarke was developed for district heating applications ($T_{out} <$ 100 °C). In the future, Heliac aims at targeting higher temperature applications, and it is expected that a modified version of the collector will be developed featuring even lower heat losses.

4. Conclusions

This study presented the world's first full-scale Fresnel lens collector field. The thermal performance of the collector field was characterized using the QDT method. It was found that the heat losses from the collectors contributed half of the total heat losses, while the piping contributed the other half. The results also showed that the peak efficiency was reduced by 11% compared to a brand-new collector, primarily due to soiling, as the collectors were not regularly cleaned.

A simulation model of the collector field was developed and validated, showing an annual heat generation of 373 kWh/m² using weather data for 2020. The model was used to conduct a sensitivity analysis to investigate the impact of key parameters on the annual heat generation. The sensitivity analysis showed that soiling had an amplified effect on the heat generation, with 11% soiling causing a 19% reduction in the annual heat generation.

For the specific operating conditions, the Fresnel lens collector field generated less heat than a comparable flat-plate collector field. However, it was shown that the collectors have low heat losses and are much less affected by the operating temperature, making them suitable for higher temperature applications. Additionally, it was found that the pressure drop in the solar field was more than an order of magnitude higher than a similar-sized flat plate collector field. This issue should be addressed in future designs of the Heliac collector, with the initial step being identifying the pressure drop of each component. Future work should also seek to elucidate the distribution of soiling on the various surfaces and the impact of cleaning.
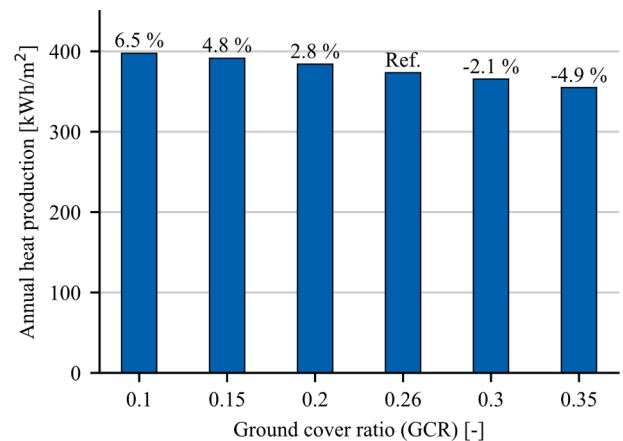

Fig. 12. Impact of GCR on the annual heat production. The percentages above each bar represent the deviation from the reference scenario.
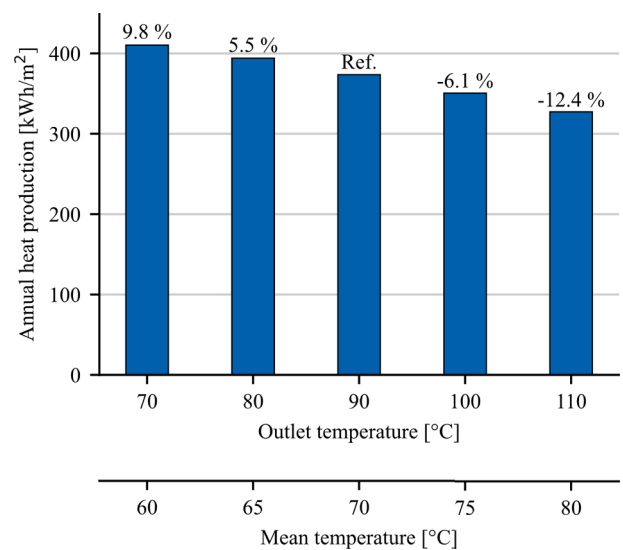

Fig. 13. Annual heat production for different mean/outlet temperatures. The percentages above each bar represent the deviation from the reference scenario.

Declaration of Competing Interest

The authors declare that they have no known competing financial interests or personal relationships that could have appeared to influence the work reported in this paper.

References

Bava, F., Dragsted, J., Furbo, S., 2017. A numerical model to evaluate the flow distribution in a large solar collector field. Sol. Energy 143, 31–42.
Bellmann, P., Wolfertstetter, F., Conceição, R., Silva, H.G., 2020. Comparative modeling of optical soiling losses for CSP and PV energy systems. Sol. Energy 197, 229–237.
Cumpston, J., Pye, J., 2014. Shading and land use in regularly-spaced sun-tracking collectors. Sol. Energy 108, 199–209.

Hersbach, H., Bell, B., Berrisford, P., Biavati, G., Horányi, A., Muñoz Sabater, J., Nicolas, J., Peubey, C., Radu, R., Rozum, I., Schepers, D., Simmons, A., Soci, C., Dee, D., Thépaut, J.-N., 2018. ERA5 hourly data on single levels from 1979 to present. Copernicus Climate Change Service (C3S) Climate Data Store (CDS).

Ibrahim, A., Sakhrieh, A., 2016. Comparative Study of Fresnel Lenses and Mirrors in Concentrated Solar Applications. In: The Fifth Global Conference on Renewables and Energy Efficiency in Desert Regions. pp. 1–7.

Imtiaz Hussain, M., Lee, G.H., 2016. Thermal performance comparison of line- and point-focus solar concentrating systems: Experimental and numerical analyses. Sol. Energy 133, 44–54.

International Organization for Standardization, 2017. ISO 9806:2017 Solar energy - Solar thermal collectors - Test methods.

Jensen, A.R., 2020. Test of Heliac 3rd Gen. Solar Collector. In: DTU Byg Report No. R-443. Technical University of Denmark.

Jensen, A.R., Sifnaios, I., Furbo, S., Dragsted, J., 2022. Self-shading of two-axis tracking solar collectors: Impact of field layout, latitude, and aperture shape. Sol. Energy.

Kumar, V., Shrivastava, R.L., Untawale, S.P., 2015. Fresnel lens: A promising alternative of reflectors in concentrated solar power. Renew. Sustain. Energy Rev. 44, 376–390.

Leutz, R., Suzuki, A., 2001. Nonimaging Fresnel Lenses: Design and Performance of Solar Concentrators. Springer-Verlag, Berlin Heidelberg.

Lin, M., Sumathy, K., Dai, Y.J., Zhao, X.K., 2014. Performance investigation on a linear Fresnel lens solar collector using cavity receiver. Sol. Energy 107, 50–62.

Miller, O.E., McLeod, J.H., Sherwood, W.T., 1951. Thin Sheet Plastic Fresnel Lenses of High Aperture. J. Opt. Soc. Am. 41 (11), 807–815.

Perini, S., Tonnellier, X., King, P., Sansom, C., 2017. Theoretical and experimental analysis of an innovative dual-axis tracking linear Fresnel lenses concentrated solar thermal collector. Sol. Energy 153, 679–690.

Qu, Z., Oumbe, A., Blanc, P., Espinar, B., Gesell, G., Klüser, L., Lefèvre, M., Saboret, L., Wald, L., Paristech, M., Observation, O.I.E.C., Antipolis, S., 2016. Fast radiative transfer parameterisation for assessing the surface solar irradiance : The Heliosat-4 method. Meteorologische Zeitschrift 26, 33–57.

Sallaberry, F., Tian, Z., Perers, B., Furbo, S., Zourellis, A., Rothmann, J.H., 2019. On-site parabolic-trough collector characterization in solar district heating plant under quasi-dynamic conditions. AIP Conf. Proc. 2126.

Tsangrassoulis, A., Doulos, L., Santamouris, M., Fontoynont, M., Maamari, F., Wilson, M., Jacobs, A., Solomon, J., Zimmerman, A., Pohl, W., Mihalakakou, G., 2005. On the energy efficiency of a prototype hybrid daylighting system. Sol. Energy 79 (1), 56–64.

Tschopp, D., Tian, Z., Berberich, M., Fan, J., Perers, B., Furbo, S., 2020. Large-scale solar thermal systems in leading countries: A review and comparative study of Denmark, China, Germany and Austria. Appl. Energy 270, 114997.

Wald, L., Lefévre, M., 2018. CAMS-72 Solar radiation products, D72.2.3.1 Regular Validation Report, S-O-N 2017.

Wang, H., Huang, J., Song, M., Hu, Y., Wang, Y., Lu, Z., 2018. Simulation and experimental study on the optical performance of a fixed-focus Fresnel lens solar concentrator using polar-axis tracking. Energies 11 (4), 887.

Xie, W.T., Dai, Y.J., Wang, R.Z., Sumathy, K., 2011. Concentrated solar energy applications using Fresnel lenses: A review. Renew. Sustain. Energy Rev. 15 (6), 2588–2606.

Yamaguchi, M., Takamoto, T., Araki, K., Ekins-Daukes, N., 2005. Multi-junction III–V solar cells: current status and future potential. Sol. Energy 79 (1), 78–85.

Zhai, H., Dai, Y.J., Wu, J.Y., Wang, R.Z., Zhang, L.Y., 2010. Experimental investigation and analysis on a concentrating solar collector using linear Fresnel lens. Energy Convers. Manag. 51 (1), 48–55.